

In-trap fluorescence detection of atoms in a microscopic dipole trap

A. J. Hilliard,^{1,2,*} Y. H. Fung,¹ P. Sompet,¹ A. V. Carpentier,^{1,3} and M. F. Andersen¹

¹*Dodd Walls Centre for Photonic and Quantum Technologies, University of Otago,
Department of Physics, P.O. Box 56, Dunedin 9016, New Zealand.*

²*Institut for Fysik og Astronomi, Aarhus Universitet, Ny Munkegade 120, 8000 Aarhus C, Denmark.*

³*Centro de Láseres Pulsados, Parque Científico, 37185 Villamayor, Salamanca, Spain.*

We investigate fluorescence detection using a standing wave of blue-detuned light of one or more atoms held in a deep, microscopic dipole trap. The blue-detuned standing wave realizes a Sisyphus laser cooling mechanism so that an atom can scatter many photons while remaining trapped. When imaging more than one atom, the blue detuning limits loss due to inelastic light-assisted collisions. Using this standing wave probe beam, we demonstrate that we can count from one to the order of 100 atoms in the microtrap with sub-poissonian precision.

PACS numbers: 37.10.De,37.10.Gh,32.50.+d,42.50.Lc

I. INTRODUCTION

Atomic ensembles stored in microscopic dipole traps provide an excellent system in which to study atomic collisions and light scattering processes. These microscopic dipole traps, so-called microtraps, enable the generation of atomic samples of very high density at modest atom number and temperature. Such a system holds the potential for generating microscopic Bose Einstein condensates [1]. Additionally, the use of Rydberg states within these small and dense atomic ensembles has applications in quantum information, such as the realization of collective qubits [2] and non-linear absorption and dispersion of light through collisions between Rydberg atoms [3, 4].

One of the key challenges in this system is the determination of the number of atoms in the microtrap. In particular, determining the atom number below the level of poissonian noise is important for realizing collective quantum gates based on Rydberg “superatoms” [2, 5]. A standard approach is to fluorescence image the atomic sample by exposing it to red-detuned optical molasses and detecting a portion of the scattered light through high numerical aperture (NA) optics [6, 7]. The laser cooling provided by the optical molasses enables an atom to scatter many photons while remaining trapped. However, the optical molasses drives light-assisted collisions that cause rapid pair-wise loss from the trap; this occurs because the red-detuned light excites a colliding pair of atoms onto an attractive molecular potential energy curve that is typically many times deeper than the optical trap [8]. This technique has been used to produce single atom occupancy in a microtrap [6, 9], but is not well-suited to the non-destructive counting of more than one trapped atom. One can avoid this loss by releasing the atoms from the dipole trap and counting the atoms once the density is sufficiently low, either in free-space [10], or by recapturing them in a larger volume trap such as a magneto-optical trap (MOT) and probing them there [11–14]. Recently, atom counting in a MOT has been demonstrated with single atom resolution for over 1000 atoms [15]. How-

ever, if the atomic sample is to be further manipulated within the microtrap, or if one wishes to count atoms in several adjacent microtraps, it would be particularly useful to employ an *in situ* method.

Here, we describe an in-trap fluorescence detection method that allows us to count one to more than a hundred atoms held in a microscopic dipole trap, thereby permitting subsequent probing of the trapped atomic cloud. This is an extension of earlier work [16], where fluorescence was induced using a standing wave of light that was blue-detuned from atomic resonance; this configuration realizes a laser cooling mechanism that works well for small detunings ($\delta \sim 2\pi \times 15$ MHz) and for intensities in excess of saturation, thereby yielding high photon scattering rates that make it ideal for fluorescence imaging. The sign of the detuning and the spatial variation of intensity lead to a form of Sisyphus cooling [17, 18] that allows an atom to remain trapped during imaging and be detected with near unit efficiency. This capability permits us to eliminate the artifacts of loss during the imaging process. For samples containing more than one atom, the small blue detuning limits the losses from inelastic light-assisted collisions, both by reducing their rate via optical shielding, and, in the case where such an inelastic collision occurs, by limiting the energy gained by the colliding atom pair to the detuning of the imaging light $\hbar\delta$ [19, 20]. We show that this method can count atoms in samples of very high density ($n \sim 5 \times 10^{13}$ cm⁻³) with sub-poissonian precision.

The paper is organized as follows. In the next section we describe the experimental setup. In section III, we summarize the methods used to calculate the light shifts of the dipole trap and probe light. Section IV describes fluorescence detection of a single atom held in a microtrap, and section V extends this to the case of multiple atoms. In section VI we present conclusions and provide an outlook for future work.

II. EXPERIMENTAL SETUP

We prepare small atomic samples by loading a microscopic dipole trap from a cloud of ⁸⁵Rb atoms held in a magneto-optical trap. Figure 1 is a schematic of the setup. The MOT operates on the $F = 3$ to $F' = 4$ transition of the D2 line

* hilliard@phys.au.dk

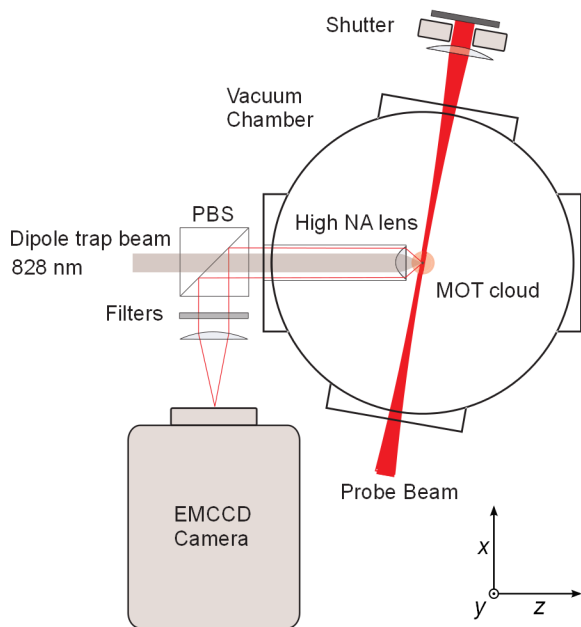


FIG. 1. (Color online) Schematic of the experimental setup. ^{85}Rb atoms are loaded from a MOT into a microscopic dipole trap. The microtrap is formed by passing 828 nm light through a high NA lens mounted inside the vacuum chamber. Atoms held in the microtrap are probed by a standing wave of light on the D1 line of ^{85}Rb . The MOT cooling beams are not shown. A portion of the light scattered by the trapped atoms is detected by an EMCCD camera.

of ^{85}Rb ($5^2\text{S}_{1/2}$ to $5^2\text{P}_{3/2}$) at wavelength $\lambda = 780$ nm. The light for the MOT is supplied as three retro-reflected beams with gaussian intensity profiles, each with spot size ($1/e^2$ waist) 6.4 mm and apertured to 7 mm in diameter; throughout the paper, we state the power measured after the apertures. A compressed MOT (CMOT) phase typically lasting 150 ms overlaps the center of the MOT cloud with the dipole trap. Subsequently, the magnetic field is extinguished and 5 ms of polarization gradient cooling leads to the loading of approximately one hundred atoms in the microtrap. The number of loaded atoms is typically varied by changing the duration of the MOT loading time (~ 1 s) and the CMOT phase. Three sets of Helmholtz coils serve to null the ambient magnetic field.

The microtrap is formed by focusing a linearly polarized gaussian beam with wavelength 828 nm by a high numerical aperture lens held in the vacuum chamber to a spot size of $w_0 = 1.8 \mu\text{m}$. The lens is a single-piece molded asphere with numerical aperture 0.55 and working distance 2.92 mm (Lightpath model 352230). The size and gaussian intensity distribution of the dipole trap beam were confirmed in a replica setup outside the vacuum chamber. These dipole beam parameters generate microscopic optical traps that are several mK deep using ~ 10 mW of optical power; a detailed description of the light shifts induced by the dipole trap beam is presented in section III.

To detect atoms in the microtrap, we induce fluorescence with a probe beam on the D1 line of ^{85}Rb . Typically, the probe

beam is blue-detuned from the $F = 2$ to $F' = 3$ transition on the D1 line ($5^2\text{S}_{1/2}$ to $5^2\text{P}_{1/2}$) for an atom at the center of the dipole trap. We choose the D1 line for imaging so that we can block stray light from the MOT and dipole trap using standard optical filters. The detuning is given by $\delta = \omega - \omega_0$, where ω is the frequency of the laser field, and ω_0 the frequency of the atomic resonance; a blue detuning corresponds to $\delta > 0$. The probe beam detuning an atom experiences depends on its position in the microtrap. In this paper, we reference the probe detuning to that experienced by an atom at the center of the dipole trap, and denote this by δ_c . The probe beam is linearly polarized (along direction y in Fig. 1) and retro-reflected to form a standing wave by a metal mirror placed outside the vacuum chamber. A mechanical shutter lies in the return beam path so that the probe beam can be toggled between traveling and standing wave configurations within the course of an experimental run. The probe beam has a gaussian intensity profile and is focused with a waist of $w_0 \cong 150 \mu\text{m}$ at the position of the atoms. We use a focused beam primarily to avoid it hitting the high NA lens so as to minimize stray light in images. Due to the available ports of the vacuum chamber, the probe beam runs at an angle of 9° to the radial axis of the dipole trap.

Given there is no cycling transition on the D1 line, we require repump light to return the atoms to the $F = 2$ ground state. For this, we primarily use the MOT cooling beams detuned by an amount $\delta_c^{33'}$ from the D2 $F = 3$ to $F' = 3$ transition for an atom at the center of the trap, averaged over the magnetic sublevels and assuming a uniform population distribution across these levels. We may also use the $F = 3$ to $F' = 2$ transition on the D1 line to optically pump the atoms back to the lower ground state. This beam shares the same optical path as the probe beam; i.e., both D1 beams propagate through the same optical fiber. Since our imaging system detects all D1 light, this repump beam increases the signal by about 80% [16]. For imaging, the D1 and D2 beams are applied with rectangular pulse envelopes.

A portion of the scattered light by the atomic sample is collected by the high NA lens and directed onto an Electron Multiplying Charge Coupled Device (EMCCD) camera. Assuming fluorescence into a solid angle of 4π , the high NA lens collects 10% of the scattered light, and half of this is reflected by a Polarizing Beam Splitter (PBS). The remaining light is optically filtered for dipole trap light at 828 nm and D2 light at 780 nm. Room light is further suppressed using shields that enclose the vacuum chamber and surrounding optics. An image is formed on the EMCCD by a high quality lens with focal length 200 mm. The combined transmission of the PBS, filters and additional optics is 37%. The EMCCD has a measured quantum efficiency of $\eta = 60\%$, so that the total detection efficiency is 2.3%. We typically operate the camera with multiplication gain set such that the total (mean) gain $G = \eta g = 20$, where the number of analog-to-digital units (ADU) and the incident number of photons are linked by $N_{\text{ADU}} = GN_{\text{ph}}$. The gain of the EMCCD is a result of several amplification stages in series leading to an additional multiplicative noise term of approximately $\sqrt{2}$ [21, 22]. The imaging system has magnification 44, and the camera has

pixel-size $16 \times 16 \mu\text{m}^2$. The image of the atomic sample is integrated over an 11×11 pixel region of interest, from which we subtract the mean background level from two ($\sim 80 \times 80$ pixel) regions on either side of the atomic signal [23].

The number of atoms held in the trap can be reduced by engaging the probe beam further blue-detuned from resonance [8]. This technique excites an atom pair onto a repulsive molecular potential curve; the energy gained by the atom pair in the process is at maximum $\hbar\delta$, in contrast to the case of excitation by a red-detuned beam. In previous work, we have achieved a single atom loading efficiency in excess of 90% [24, 25]. In this paper, we study the imaging of single atoms produced by this technique, but we also employ it to obtain a single atom fluorescence signal as a reference level when imaging multiple trapped atoms.

III. LIGHT SHIFTS

The use of a deep dipole trap to hold an atomic sample means that the atoms can scatter many photons and remain trapped, but it also requires us, when imaging, to take account of the significant light shifts induced by the microtrap [26]. Furthermore, the blue Sisyphus mechanism used for probing relies on the spatial variation of the light shifts induced by the standing wave probe beam, so an accurate calculation of these shifts is critical to analyzing this mechanism applied to in-trap fluorescence detection. Our approach is to calculate the light shifts generated by the dipole trap and to include these as effective spatially dependent detunings in the calculation of the light shifts due to the probe beam. This approach is valid and convenient because the large detuning from any optical transition of the dipole trap light means that the dressed states within the dipole trap are very well approximated by the bare atomic states with shifted energy levels [27].

We calculate the light shifts induced by the dipole trap in a semi-classical picture where an applied laser beam is represented by a classical electric field $E(\mathbf{r}) \cos(\omega t)$. To second order in perturbation theory, the shift of atomic level $|i\rangle$ is given by [28]

$$\Delta E_i(\mathbf{r}) = \frac{|E(\mathbf{r})|^2}{4\hbar} \sum_{j \neq i} |M_{ij}|^2 \left(\frac{1}{\omega - \omega_{ij}} - \frac{1}{\omega + \omega_{ij}} \right), \quad (1)$$

where the sum is taken over all other electronic states $|j\rangle$, and $M_{ij}(\omega_{ij})$ denotes the dipole matrix element (atomic transition frequency) between states $|i\rangle$ and $|j\rangle$. If the frequency of the applied field is close to a given atomic transition, the rotating-wave approximation may be applied and the second term in parenthesis in Eq. (1) may be discarded, leaving the denominator as the detuning from the chosen transition $\delta = \omega - \omega_{ij}$.

To calculate the light shifts for ^{85}Rb , we use values for the dipole matrix elements and bare atomic transition frequencies [29] to perform the sum in Eq. (1) over the relevant dipole allowed transitions on the D1 and D2 lines [30]. The electric field strength is related to the intensity by $I(\mathbf{r}) = \frac{1}{2}c\epsilon_0 |E(\mathbf{r})|^2$. The gaussian intensity distribution of the dipole trap beam is $I(\mathbf{r}) = I_0 \exp(-2r^2/w(z)^2)$, where

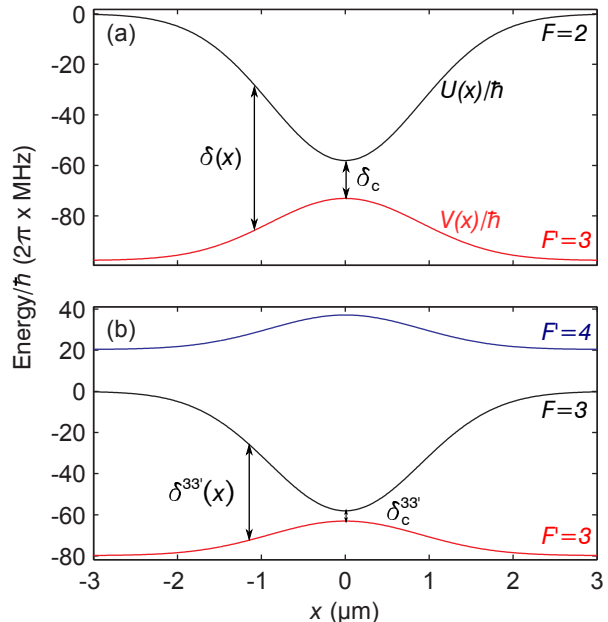


FIG. 2. (Color online) Light shifts for relevant states of ^{85}Rb along the radial direction of the microtrap at a power of 20 mW. (a) States addressed by D1 probe beam: Ground state $F = 2$ (black line) and excited state $F' = 3$ (red line). The probe beam optical frequency ω has been subtracted from the excited state energy. δ_c is the detuning of the probe beam at the center of the microtrap. Away from the center, an atom experiences a position-dependent detuning $\delta(x)$ that is larger than δ_c . (b) States addressed by the D2 MOT cooling beams: Ground state $F = 3$ (black line) and excited states $F' = 3$ (red line) and $F' = 4$ (blue line). The MOT cooling beams optical frequency ω_{D2} has been subtracted from the excited state energies. The magnetic sublevels in the excited states on the D2 line experience different light shifts; the curves show the mean across the magnetic sublevels. $\delta_c^{33'}$ denotes the detuning of the MOT cooling beams from the $F = 3 \rightarrow F' = 3$ transition on the D2 line at the center of the microtrap, with $\delta^{33'}(x)$ the position dependent detuning.

$I_0 = 2P/(\pi w(z)^2)$, P is the beam power, and the position dependent spot size is given by $w(z) = w_0 [1 + (z/z_R)^2]^{1/2}$, with $z_R = \pi w_0^2/\lambda$ the Rayleigh range.

Figure 2 shows light shifts calculated using Eq. (1) for relevant states in ^{85}Rb along the radial direction of the dipole trap beam. The red detuning ($\delta < 0$) of the dipole trap beam shifts the ground states down and the excited states up. Figure 2(a) shows the light-shifted energies of the states addressed by the D1 probe beam. Due to the use of linearly polarized light, the magnetic sublevels of the ground states $F = 2, 3$ and the excited states $F' = 2, 3$ on the D1 line are shifted equally. We denote the energy of the lower ground state $U(\mathbf{r})$ and the $F' = 3$ excited state on the D1 line $V(\mathbf{r})$. For 20 mW power in the dipole trap beam, $[V(0) - U(0)]/\hbar = 2\pi \times 82.7$ MHz. The microtrap leads to a position dependent detuning $\delta(\mathbf{r}) = \delta - [V(\mathbf{r}) - U(\mathbf{r})]/\hbar$ for the probe beam. Figure 2(b) shows the light-shifted en-

ergies of the states addressed by the MOT cooling beams on the D2 line: The $F = 3$ ground state and the $F' = 3, 4$ excited states. The light shifts for the excited states on the D2 line are m_F -level dependent; the curves show the mean over the magnetic sublevels, assuming a uniform population distribution across them. As for the probe beam, the microtrap leads to a position dependent detuning for the MOT cooling light from the $F = 3$ to $F' = 3$ transition, $\delta^{33'}(\mathbf{r})$. However, on the D2 line, the situation is complicated by the fact that as the atom moves away from the center of the trap, the $F = 3$ to $F' = 4$ transition also becomes near-resonant.

To calculate the energy shifts of the atom due to the probe beam we use the dressed atom approach [17]. For fluorescence imaging, the atoms are exposed to a standing wave of light that is near-resonant with the $F = 2$ to $F' = 3$ transition on the D1 line. Given the small detuning, we approximate the system as a two-level atom exposed to a single mode light field, described within the electric dipole and rotating-wave approximations; i.e., the Jaynes-Cummings model [31]. To account for the light shifts induced by the dipole trap, we use the position dependent probe detuning $\delta(\mathbf{r})$ in the calculation of the dressed states. Our standard imaging conditions use $\delta_c \approx 2\pi \times 15$ MHz and an intensity higher than the on-resonance saturation intensity. The dressed state energies of the combined light-atom system are [17]

$$\begin{aligned} E_{1n}(\mathbf{r}) &= (n+1)\hbar\omega + U(\mathbf{r}) - \frac{\hbar\delta(\mathbf{r})}{2} + \frac{\hbar\Omega(\mathbf{r})}{2}, \\ E_{2n}(\mathbf{r}) &= (n+1)\hbar\omega + U(\mathbf{r}) - \frac{\hbar\delta(\mathbf{r})}{2} - \frac{\hbar\Omega(\mathbf{r})}{2}, \end{aligned} \quad (2)$$

where n is the number of photons in the light field. The generalized Rabi frequency is given by $\Omega(\mathbf{r}) = [\delta(\mathbf{r})^2 + \omega_1^2(\mathbf{r})]^{1/2}$, with the on-resonance Rabi frequency $\omega_1(\mathbf{r})$ in the semi-classical picture defined by $\omega_1(\mathbf{r})e^{i\phi(\mathbf{r})} = M_{ij} \cdot E(\mathbf{r})/\hbar$, where $\phi(\mathbf{r})$ is the phase of the light-atom coupling.

Figure 3 shows the dressed state energies for a ^{85}Rb atom held in the dipole trap, exposed to the standing wave probe beam with power $30 \mu\text{W}$ and $\delta_c = 2\pi \times 15$ MHz. For simplicity, we treat the probe beam as propagating orthogonal to the dipole trap beam. With the choice of a small blue detuning for an atom at the center of the trap, the effective detuning of the probe beam increases away from the center. Thus, at the center of the trap, the effective probe beam detuning is minimal and the light shift induced by the probe beam is maximal. Away from the center, the effective blue detuning increases and the probe beam light shifts decrease in magnitude.

IV. SINGLE ATOM DETECTION

Our main goal in single atom fluorescence detection is to detect as much light scattered by the atom as possible while leaving it trapped. As such, the two quantities we use to characterize the detection performance are the integrated fluorescence – the number of ADUs we detect on the camera – and the retention probability – the probability that a single atom

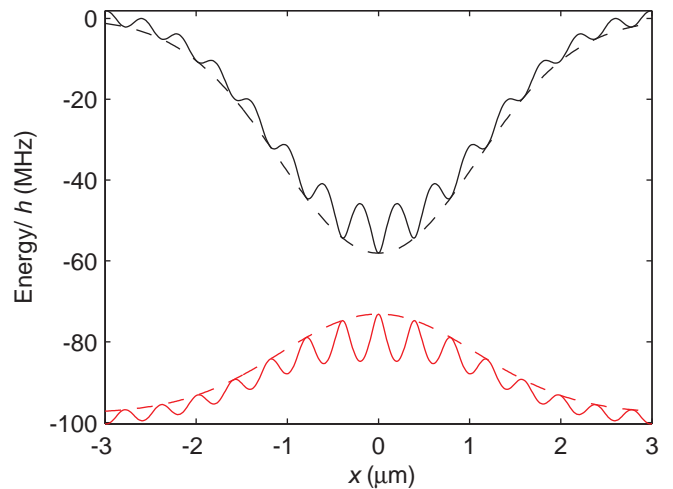


FIG. 3. (Color online) Calculated dressed state energy for an atom in the microtrap dressed by a standing wave of near-resonant light. The probe beam has power $30 \mu\text{W}$ and $\delta_c = 2\pi \times 15$ MHz. The ground state $F = 2, m_F = 0$ is shifted down by the dipole trap (black dashed line), and modulated by a standing wave of blue-detuned light on the D1 line (black solid line). The excited state $F' = 3, m_F = 0$ is shifted up by the dipole trap (red dashed line), and modulated by the standing wave (red solid line).

remains in the microtrap following a fluorescence image. The retention probability is a measure of the heating caused by the detection process. The higher the single atom scattering rate, the higher the integrated fluorescence signal and the greater the accuracy with which we can distinguish between the presence and absence of an atom in the microtrap. The integrated fluorescence and the retention probability are coupled in the sense that a low retention probability leads to the loss of an atom from the microtrap during the detection process, and thereby a lower signal than if the atom had remained trapped throughout the exposure.

Figure 4(a) is a schematic of the experimental sequence we use to investigate fluorescence detection of a single atom held in the microtrap. The sequence begins by loading ~ 100 atoms into the microtrap from the MOT, whereupon we drive inelastic light-assisted collisions to reduce the number of atoms in the trap to one or zero [24, 25]. The first fluorescence image confirms the presence of an atom. For this image, the probe beam is applied as a standing wave with $30 \mu\text{W}$ power and detuning $\delta_c = 2\pi \times 15$ MHz, and the D2 beams each has power 1.4 mW and detuning $\delta_c^{33'} = 2\pi \times 2.8$ MHz. By this imaging procedure, an atom is retained in the microtrap with 99% efficiency. In the second ‘variable’ image, an imaging parameter is varied, and the integrated fluorescence for this setting is recorded. The third image, identical in parameters to the first, tests whether the atom is still trapped after the second image. The outcome of the third image, conditioned on there being an atom present in the first image, gives the retention probability. All images have 10 ms exposure time. Unless otherwise stated, each data point shows the mean of 200 (unconditioned) experimental runs and error bars show the standard error of the mean; to avoid obtaining unphysical

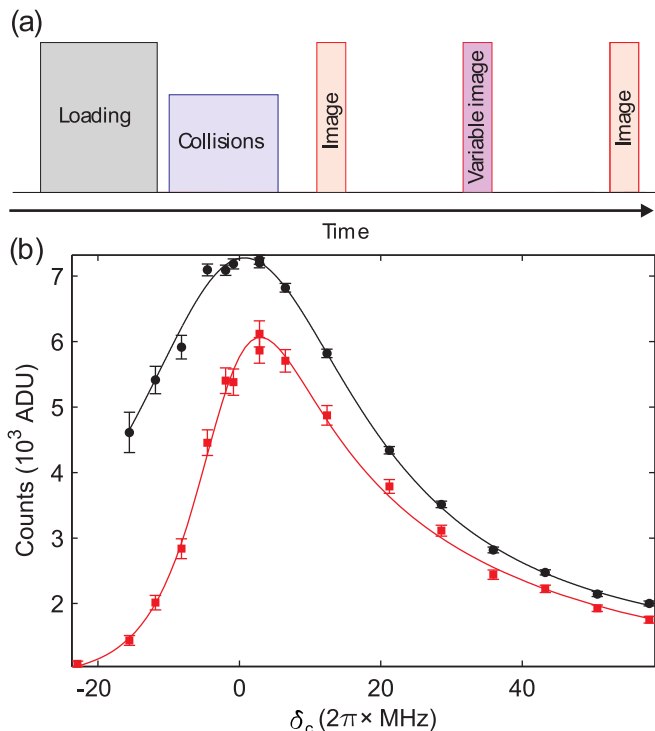


FIG. 4. (Color online) (a) Experimental sequence to investigate the fluorescence detection of a single atom. (b) Fluorescence spectrum observed when the probe beam detuning is varied. Integrated fluorescence conditioned on the detection of a single atom in the first and third image (black circles), data conditioned only on there being an atom in the first image (red squares). Solid lines are fits of asymmetric Lorentzian functions to the data.

retention probabilities exceeding 100%, we do not correct for the small loss induced by the first and third images when calculating the probability of retaining an atom. With a view to presenting qualitative arguments to describe single atom detection, we simplify the physical picture by omitting the D1 repump light on the $F = 3$ to $F' = 2$ transition. The addition of the D1 repump light does not change the performance of the fluorescence detection other than to increase the observed signal, a feature we make use of when imaging samples containing several atoms (see section V).

To investigate the characteristics of the blue Sisyphus mechanism as a function of detuning, and to confirm the light shift calculations of section III, we performed an in-trap fluorescence spectrum of a single atom. To do this, we varied the detuning of the probe beam in the ‘variable image’ in the experimental sequence (see Fig. 4(a)), while holding the power at $30 \mu\text{W}$. The MOT cooling beams were set to $\delta_c^{33'} = -2\pi \times 5 \text{ MHz}$ and 1.4 mW per beam. Figure 4(b) shows the observed single-atom spectrum. The red squares show the mean integrated fluorescence for the experimental runs where there was an atom present in the first image. The black circles show the mean integrated fluorescence conditioned on there being an atom present both in the first and third images. The two data sets have been fitted with an asymmetric Lorentzian model [32]. The unconditioned data is asymmet-

ric because the standing wave probe beam has a cooling effect on the blue side of the spectrum and a heating effect on the red side. This sign dependence of the detuning also shifts the peak of the unconditioned data approximately 3 MHz to the blue. In contrast, the peak of the conditioned data agrees well with $\delta_c = 0$, confirming the validity of the light shift calculation. This illustrates a great advantage of non-destructive imaging at the single atom level: It allows one to identify artifacts from features. In this case, we avoid the corruption of the spectroscopic signal due to atom loss.

The Sisyphus mechanism realized by the standing wave probe beam cools an atom for blue detunings and heats for red detunings [17], so it is somewhat surprising that for modest red detunings of the probe beam, $-2\pi \times 15 \lesssim \delta_c < 0 \text{ MHz}$, an atom remains trapped in some of the experimental runs. There are two reasons for this, both relating to the position of the atom in the microtrap and the effect this has on the frequency of the applied light fields for probing and optical pumping. First, the effective probe beam detuning is pushed to the blue as an atom travels into the wings of the microtrap. As such, although the standing wave probe beam heats an atom at the center of the trap for $\delta_c \approx -2\pi \times 15 \text{ MHz}$, in the wings the effective blue detuning is restored and the atom experiences the blue Sisyphus cooling mechanism, thereby remaining trapped. Second, the MOT cooling beams laser cool a trapped atom when it moves to the wings of the microtrap: Although tuned so as to optically pump an atom at the center of the trap back to the $F = 2$ ground state, i.e., $\delta_c^{33'} \approx 0$, away from the center of the microtrap, an atom experiences the MOT cooling beam frequency closer to the $F = 3$ to $F' = 4$ cycling transition, thereby realizing a standard red-detuned optical molasses. As such, an atom can be heated at the center of the trap by the probe beam, but be cooled by the MOT beams in the wings of the microtrap so that it remains trapped.

This shows that it is important to characterize the role the MOT cooling light plays in the detection process, even though its nominal role is to optically pump a trapped atom to the electronic ground state addressed by the probe beam. To do this, we varied the detuning of the MOT cooling light while keeping the D1 imaging parameters constant. The experiment was performed for standing and traveling wave probe beams in the second image in order to test the cooling effect of the MOT cooling light in the presence and absence of the Sisyphus cooling mechanism. As noted above, the blue Sisyphus cooling mechanism relies on the spatial modulation of the probe beam intensity: In a traveling wave configuration, the probe beam has a flat intensity distribution over the extent of the microtrap and therefore provides no cooling. Figure 5(a) shows the probability of detecting an atom in the third image, conditioned on it being detected in the first. For both standing and traveling wave detection and $\delta_c^{33'} \geq -2\pi \times 5 \text{ MHz}$, the retention probability is in excess of 97%. However, below this detuning, both standing and traveling wave probe beams show an approximately linear decrease in retention probability, but the decrease is much sharper for the traveling wave case. Thus, for $\delta_c^{33'} \geq -2\pi \times 5 \text{ MHz}$, the D2 beams perform enough laser cooling to keep an atom trapped while imaging

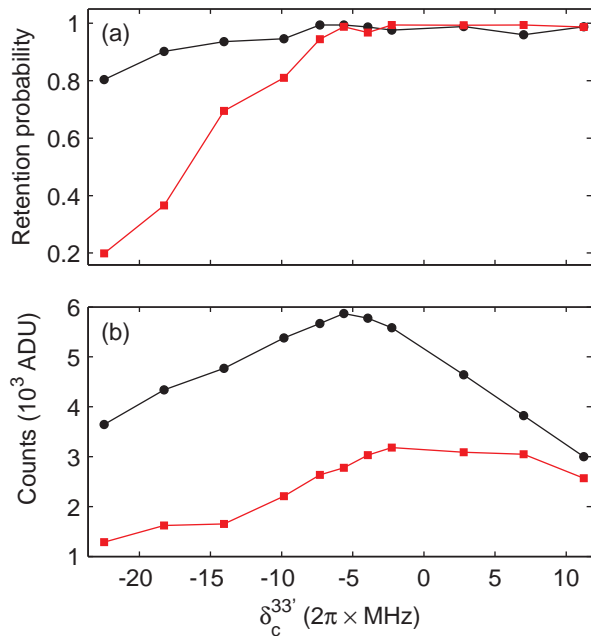


FIG. 5. (Color online) Imaging performance as a function of MOT cooling light detuning from $F = 3$ to $F' = 3$, $\delta_c^{33'}$, at constant MOT cooling light power. The experiment was performed using standing wave (black circles) and traveling wave (red squares) probe beams. (a) Probability of retaining an atom in the microtrap. (b) Integrated fluorescence.

for this choice of probe beam parameters, whereas below this detuning, the blue Sisyphus cooling mechanism of the probe beam is necessary to keeping the atom trapped. Figure 5(b) shows the integrated fluorescence counts of the second image. In the standing wave case, the counts are maximized for $\delta_c^{33'} = -2\pi \times 5$ MHz.

To investigate this imaging process further, we scanned the probe beam power for several values of detuning. In order to focus on the cooling effect of the blue Sisyphus mechanism, the D2 light was set to $\delta_c^{33'} = -2\pi \times 10$ MHz with 1.4 mW per beam. This value of the detuning was a compromise between accentuating the cooling effect of the standing wave probe beam, and ensuring efficient optical pumping and hence a good signal. Figure 6 shows the retention probability and integrated fluorescence for three values of the probe beam detuning: $\delta_c = 2\pi \times 5$, 15 and 35 MHz.

The retention probability shows an interesting structure for the low detuning $\delta_c = 2\pi \times 5$ MHz, which is approximately equal to the natural linewidth $\Gamma_{D1} = 2\pi \times 5.75$ MHz of the transition. For zero power, the retention probability is of course approximately one, limited only by the performance of the first and third images. However, as the power of the probe beam is increased very slightly, the retention probability drops sharply and reaches a local minimum at a power of $2.5 \mu\text{W}$, corresponding approximately to saturation intensity I_{sat} for the transition. As the power is further increased, the retention probability increases to a peak value and eventually begins to

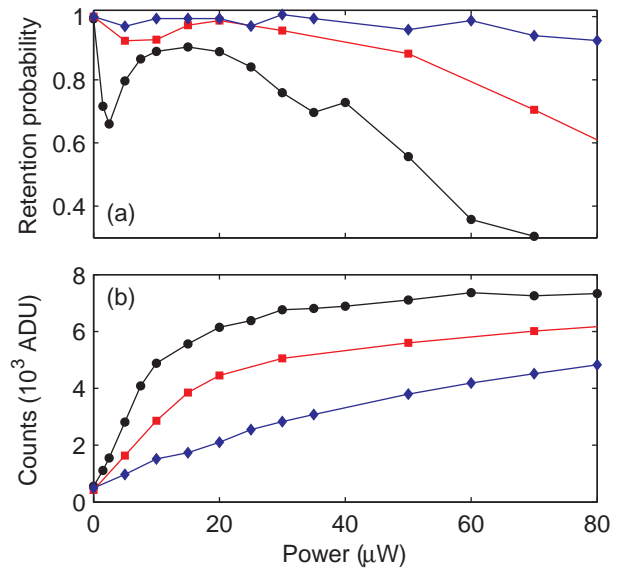


FIG. 6. (Color online) Single atom detection as a function of probe beam power for three detunings $\delta_c = 2\pi \times 5$ (black circles), 15 (red squares) and 35 (blue diamonds) MHz. (a) Probability of retaining an atom in the microtrap. (b) Integrated fluorescence.

decrease. The initial drop at low power can be understood as Doppler heating predominating over the Sisyphus mechanism. To give a qualitative picture of this behaviour, we argue using the simple treatment of Doppler heating/cooling, where the total force on an atom due to a counter-propagating pair of laser beams is given by the sum of the contribution from each beam [33]. Using this description, the Doppler heating rate attains its maximum value for $\delta_c = \Gamma_{D1}$ and $I = I_{\text{sat}}$. Above $2.5 \mu\text{W}$, the Doppler heating rate decreases and the cooling effect of the blue Sisyphus mechanism increases as the magnitudes of the dressed state energies increase at the anti-nodes of the standing wave. The minimum temperature achievable with the blue Sisyphus mechanism is proportional to the modulation amplitude of the dressed states E_{mod} in the standing wave [34]; as the power is further increased, the temperature of the sample increases and eventually becomes commensurate with the trap depth, so that the D2 cooling beams can no longer provide enough cooling to keep the atom trapped. If one assumes a Maxwell-Boltzmann distribution for the energy of an atom with temperature $T \sim E_{\text{mod}}/K_B$ in the microtrap, integrating the distribution from zero to U_0 shows the same trend as this experimental retention probability.

At higher blue detunings, the dip in retention probability at low power is significantly reduced: $\delta_c = 2\pi \times 15$ MHz shows a small decrease at $10 \mu\text{W}$, and at $\delta_c = 2\pi \times 35$ MHz the retention probability is essentially flat for low power. This can be understood from the fact that for detunings larger than the natural linewidth, the peak Doppler heating rate shifts to higher intensities, where the modulation of the dressed state energies (Eq. (2)) is already significant, and thus the cooling effect of the blue Sisyphus mechanism predominates over Doppler heating.

V. MULTI-ATOM DETECTION

In Fig. 4, we saw that trap loss can distort the fluorescence signal of a single atom. However, due to the fact that one atom can be detected with near-unit efficiency, this loss effect could be eliminated by adding additional pictures to the experimental sequence and appropriate post-processing. In the case of fluorescence detection of multiple atoms in a microscopic volume, the process is complicated by rapid two-body loss due to light-assisted collisions between atoms. In previous work [16], we showed that fluorescence imaging using a blue-detuned standing wave of light could be used to count three atoms held in a microtrap based on the unambiguous signature of steps in the integrated fluorescence. However, this signature is lost when counting larger atomic samples because light-assisted collisions reduce the atom number during a given exposure time, thereby blurring the steps in fluorescence. Thus, to accurately count multiple atoms in a microscopic volume, we must devise additional techniques to mitigate the effects of loss during the imaging sequence.

In our system, inelastic light-assisted collisions during fluorescence imaging are the dominant loss mechanism. In general, binary collisions between cold alkali atoms in their electronic ground states occur through an induced dipole-dipole interaction, a second order effect with interaction energy given by C_6/R^6 , where R is the inter-atom distance and C_6 is the van der Waals interaction coefficient [8]. In the presence of near-resonant light, the electronic excited state population is non-zero and atoms can interact via a resonant dipole interaction C_3/R^3 . One can estimate the inter-atom distance at which the light is resonant with the two-atom system, the Condon point R_C , by $\hbar\delta = C_3/R_C^3$. A typical C_3 value is $20 \text{ eV}\text{\AA}^3$, so for $\delta = 2\pi \times 15 \text{ MHz}$, $R_C \sim 500 \text{ \AA}$. For 100 atoms in the microtrap at $160 \text{ }\mu\text{K}$, the peak density is $n_0 \sim 5 \times 10^{13} \text{ cm}^{-3}$, and the mean inter-atom distance is $R \sim n_0^{-1/3} \sim 250 \text{ \AA}$. Thus, in this system the mean inter-atom distance is of the same order as the interaction length, and light-assisted collisions predominate.

Our approach to counting atoms in mesoscopic samples is to model the effect of two- and one-body loss on the time-resolved integrated fluorescence and from this determine the atom number as a function of imaging time. A similar approach using standard red-detuned cooling light was recently demonstrated for up to ~ 20 atoms in a larger volume dipole trap [5]. We model the atom loss during imaging with a master equation, in which the time evolution of the probability p_N to obtain N atoms in the microtrap is given by [35, 36]

$$\frac{dp_N}{dt} = \beta(\mathbb{E}^2 - \mathbb{1}) \left[\frac{N(N-1)}{2} p_N \right] + \gamma(\mathbb{E} - \mathbb{1})[N p_N], \quad (3)$$

where β and γ are the two-body and one-body decay rates, respectively, and \mathbb{E} is the step operator. This operator is defined by its effect on a function $f(N)$ by $\mathbb{E}[f(N)] = f(N+1)$ and $\mathbb{E}^{-1}[f(N)] = f(N-1)$. The first term in Eq. (3) describes a two-body loss process, where both atoms are lost from the trap; we call this ‘‘process 2’’. One can also model a two-body collision where only one atom is lost from the trap (‘‘process

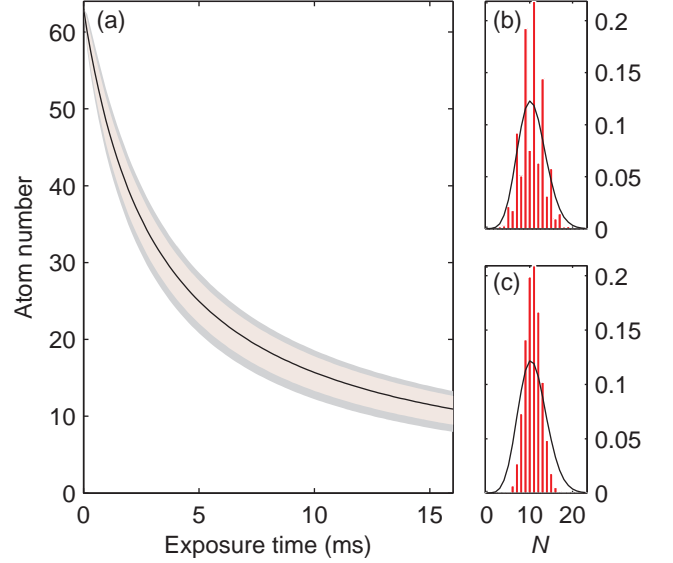


FIG. 7. (Color online) Atom number distributions evaluated for processes 1 and 2 from Eq. (3) using $N_0 = 63$, $\beta = 4.9 \text{ s}^{-1}$ and $\gamma = 0.97 \text{ s}^{-1}$. To ensure the same mean atom number for the two processes, we use β for process 2 and 2β for process 1 (see Eq. (4) and associated text). (a) Mean atom number (black line) calculated from Eq. (4) assuming $\beta\Delta N^2 = 0$. The shaded regions indicate the 2σ width of the atom number distributions for process 2 (gray) and 1 (red). (b) Atom number distribution at 16 ms for process 2. The solid line shows the poissonian distribution for the mean atom number $\bar{N} = 10.6$. (c) Same as (b) but for process 1.

1’’) by replacing \mathbb{E}^2 in this term by \mathbb{E} ; in our experiments, such a process arises from the combined effect of the imaging beam and the MOT cooling beams used to optically pump the atoms. By probing an atomic sample containing just two atoms, we find that process 1 and process 2 occur with approximately equal probability. Equation (3) comprises a system of equations that may be solved numerically for samples containing several hundred atoms.

The time evolution of the mean number of atoms, $\bar{N} = \sum_{N=0}^{\infty} N p_N$, may be found from Eq. (3), yielding

$$\frac{d\bar{N}}{dt} = -\beta\bar{N}(\bar{N} - 1) - \gamma\bar{N} - \beta\Delta N^2, \quad (4)$$

where ΔN^2 is the variance in the atom number. Equation (4) also describes process 1, but in this case the first term on the right hand side reads $-\frac{\beta}{2}\bar{N}(\bar{N} - 1)$, given that only one of the two atoms is lost from the trap. Accordingly, to achieve the same mean decay rate when comparing the two processes, we use decay rate β for process 2, and 2β for process 1.

Figure 7 shows the time evolution of the atom number distribution calculated using Eq. (3) for representative parameters used in our experiments. Beginning from 63 atoms in the trap, the imaging leads to a decrease in the mean number of atoms and an increase in the atom number variance. Figure 7(a) shows \bar{N} as a function of exposure time and the shaded regions denote the 2σ width of the atom number dis-

tribution for processes 1 and 2. The solid line shows the mean atom number calculated from Eq. (4) and assuming $\beta\Delta N^2 = 0$; it is clear that this solution approximates the means of the two distributions very well, showing that this correction to the mean atom number is negligible for our experimental parameters. The atom number variance initially grows from its (idealized) value of zero at $t = 0$ to reach its “limiting” value at $t \approx 10$ ms. This value is determined by the competition between the one and two-body loss mechanisms: Acting alone, the former leads to a poissonian number fluctuations, i.e., $\Delta N^2 = \bar{N}$, whereas process 2 induces an atom number variance of $0.667\bar{N}$ for $\bar{N} \gtrsim 10$ [37], reducing to $\Delta N^2 = 0.5\bar{N}$ for the special case of $\bar{N} = 0.5$ [6]. Process 1, on the other hand, leads to zero atom number variance in the limit that $\bar{N} \rightarrow 1$, because the reduction in atom number stops when there is only one atom left in the trap. The differences in the atom number variance produced by these two-body processes are evident in Figs. 7(b) and (c), which show the atom number distributions at $t = 16$ ms for process 2 and 1, respectively. Process 1 induces a smooth, unimodal distribution, whereas process 2 yields a jagged distribution with a unimodal envelope. For this calculation, odd atom numbers are more probable because the initial atom number was chosen to be odd, and process 2 leads to pairwise loss. In both cases, however, the width of the distribution is smaller than a poisson distribution with the same mean.

A. Mean values

This discussion shows that to determine the mean number of atoms in the trap, we may solve Eq. (4) under the condition that the atom number variance term is neglected. We will return to the fluctuations about the mean atom number in section V B, where we quantify the precision of the imaging method. As noted above, the choice of process 1 or 2 does not affect the description of the mean atom number other than the fitted value of β . To simplify the comparison of our method with standard fluorescence detection methods, we model the mean value data with process 2. The solution of Eq. (4) within the approximation that $\beta\Delta N^2 = 0$ is given by

$$\bar{N}(t) = \frac{e^{At}}{\frac{\beta}{A}(e^{At} - 1) + \frac{1}{N_0}}, \quad (5)$$

where $A = \beta - \gamma$ and N_0 is the initial atom number. In an experiment, we detect the amount of light scattered by the atomic sample

$$F_{\text{int}}(t) = \int_0^t F_1 \bar{N}(t') dt', \quad (6)$$

where we have assumed that the integrated fluorescence is given by the product of the single atom fluorescence rate F_1 , which is assumed to be constant in time, and the number of trapped atoms. Performing the integration, we obtain

$$F_{\text{int}}(t) = \frac{F_1}{\beta} \ln \left[\frac{\beta N_0 (e^{At} - 1)}{A} + 1 \right]. \quad (7)$$

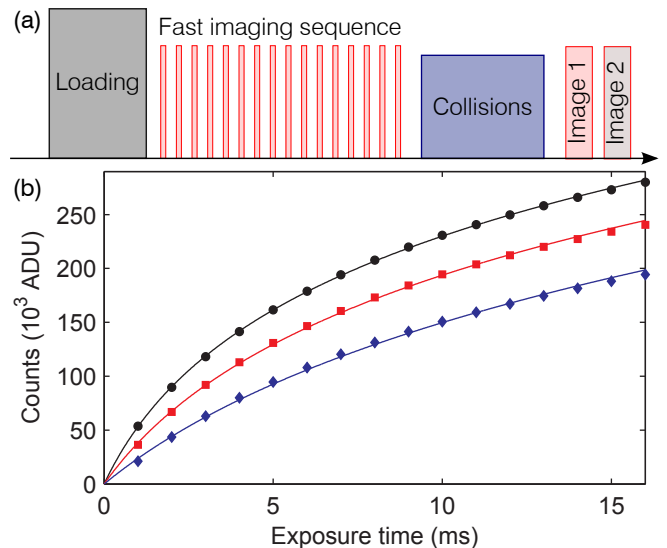


FIG. 8. (Color online) (a) Experimental timeline for multi-atom detection. (b) Integrated fluorescence as a function of exposure time for three values of the initial atom number N_0 . Each data set was fitted with Eq. (7) using F_1 and γ as fixed input parameters (see text). The fitted parameters were: (black circles) $N_0=85.9(5)$, $\beta = 6.41(4)\text{s}^{-1}$; (red squares) $N_0=58.4(4)$, $\beta = 6.00(5)\text{s}^{-1}$; (blue diamonds) $N_0=31.3(3)$, $\beta = 5.70(9)\text{s}^{-1}$. The number in parenthesis gives the uncertainty from the fitting routine in the least significant figure.

Thus, to determine the initial atom number of a trapped sample, we take in-trap fluorescence images for several values of exposure time and use Eq. (7) to model how the integrated fluorescence changes in time.

Figure 8(a) is a schematic of the experimental sequence used to determine the number of atoms held in the microtrap. We achieve a given initial atom number N_0 by varying parameters in the MOT and CMOT phases; through this loading procedure and evaporation, the atomic clouds thermalize to a temperature $T \sim 160 \mu\text{K}$ [38]. The time dependence of F_{int} is probed by exposing the trapped sample to several short pulses of imaging light and recording the fluorescence on the EMCCD camera. For this fast imaging sequence, the camera is operated in kinetics mode and the camera chip masked such that we can take ~ 20 frames for our chosen region of interest. Each imaging pulse has 1 ms duration, with a 22 ms delay between frames. F_{int} is generated by taking the cumulative sum of the integrated signal for each frame [39]. In order to measure F_1 , at the end of the fast imaging sequence we drive light-assisted collisions with the probe beam set to reduce the trapped atom number to zero or one [24, 25], whereupon we take a 10 ms fluorescence image (“Image 1” in Fig. 8(a)) using the same parameters as for the fast imaging sequence. Finally, a standard image (“Image 2”) of duration 10 ms determines with near unit efficiency whether there was zero or one atom held in the microtrap in “Image 1”. Using the final two images, and averaging over several experimental runs, we obtain the fluorescence rate for one or zero atoms, allowing us to calculate the background subtracted single atom fluorescence

rate F_1 and the background subtracted integrated fluorescence F_{int} . The use of collision beam parameters to produce 50% zeros and ones minimizes the statistical error in the measured background subtracted single atom fluorescence rate, meaning that one could also employ the standard approach of using light-assisted collisions driven by red-detuned molasses for this step.

Figure 8(b) shows the integrated fluorescence as a function of exposure time for three values of the initial atom number N_0 . The experiment was performed for a dipole trap power of 30 mW, yielding a trap depth of $U_0 = h \times 87.1 \text{ MHz} = K_B \times 4.18 \text{ mK}$, with standing wave probe beam parameters $\delta_c = 2\pi \times 15 \text{ MHz}$ and power 40 μW for both the $F = 2 \rightarrow F' = 3$ and $F = 3 \rightarrow F' = 2$ D1 transitions, and MOT cooling beam parameters $\delta_c^{33'} = -2\pi \times 6 \text{ MHz}$ at 0.6 mW per beam. The data has been fitted with Eq. (7), using F_1 and γ as fixed parameters. The single atom decay rate was measured to be $\gamma = 0.97 \text{ s}^{-1}$ in a separate experiment where a single atom was prepared in the microtrap and exposed to the same imaging conditions as we use for N -atom samples. The initial slope of the integrated fluorescence for each data set is given by $N_0 F_1$. For longer exposure times, the fluorescence rate decreases as a result of the loss of atoms from the trap during imaging. It is evident that Eq. (7) models the experimental data very well, yielding measured initial atom numbers of 31, 58 and 86 for the three data sets. We have verified the method for initial atom numbers up to 130, which is approximately the highest number of atoms we obtain in the microtrap using the described loading procedure.

The measured values of two-body loss rate are significantly smaller than those reported for comparable experiments that use red-detuned imaging light. Our low value of β arises from the fact that the probe beam is blue-detuned with respect to the primary transition used for imaging: The blue detuning excites the colliding atoms onto a repulsive molecular potential curve [19], which limits trap loss due to inelastic light-assisted collisions by ensuring that the maximum energy the atom pair gains is $\hbar\delta$; for our experimental parameters, this gained energy is significantly smaller than the trap depth. In order to compare the measured values of β with those from other experimental configurations, we calculate the normalized two-body loss rate $\beta_{\text{norm}} = \beta 2\sqrt{2}V$, where $V = (2\pi K_B T / (m\bar{\omega}^2))^{3/2}$ is the volume occupied by the sample at temperature T , $\bar{\omega}$ is the geometric mean of the trapping frequencies, and m is the atomic mass [40]. From Fig. 8, we measure a typical value $\beta = 6 \text{ s}^{-1}$, which in normalized form reads $\beta_{\text{norm}} = 1.4 \times 10^{-11} \text{ cm}^3 \text{ s}^{-1}$. For comparable experiments using red-detuned fluorescence imaging light, the normalized two-body decay rate is typically two orders of magnitude larger [41]. In particular, we find $\beta_{\text{norm}} = 1.4 \times 10^{-9} \text{ cm}^3 \text{ s}^{-1}$ for the experiment described in Ref. [5]. It is this feature of our imaging technique that permits the determination of atom number in samples of very high density.

In our treatment, we assume that the single atom fluorescence rate F_1 does not depend on the atom number. This assumption may lead to systematic errors for very dense samples. In particular, light scattering may be suppressed due

to dipole-dipole interactions [42] or if the temperature of the atoms is number dependent. The latter would lead to a number dependent broadening of the transition due to the trap light shifts. An atom number dependent temperature could arise due to heating from inelastic collisions that release a low energy such that the colliding atoms are not lost. Inclusion of 3-body processes in the model (Eqs. (4) to (7)) did not improve the fit in Fig. 8(b), but for higher densities they may also play a role. Reference [5] demonstrated that the atom number in small samples can be determined from the Rabi frequency of collective Rydberg excitations, which may provide a method for detecting potential systematic errors in our parameter regime. However, in the following section we present a noise model for the imaging process which builds on the fitted values of N_0 and β . This model contains no additional free parameters and shows very good agreement with the experimental data, thereby supporting the accuracy of the method.

B. Fluctuations

In this section, we develop a noise model to characterize the imaging method described above, thereby extending the method from the mean atom number to the atom number distribution within the microtrap. Similar to previous work [15, 43], we characterize the noise properties of the imaging method by calculating the two-sample variance from the atom number measured by two consecutive imaging pulses: $\sigma^2 = \frac{1}{2} \text{var}(N_2 - N_1)$. Contrary to previous work, however, we calculate the noise model based on the full solution of the master equation, and use no free parameters to fit the noise model to the data. We also compare the atom number at the end of the first imaging pulse N_1 with the atom number at the beginning of the second imaging pulse N_2^0 . Such an imaging procedure is experimentally relevant, allowing one to determine the atom number in the microtrap, perform an experiment in which the atom number changes, and finally measure the number of atoms remaining in the trap. In light of the discussion of Eq. (3), one may also view the imaging process as a method to prepare an atomic sample with an atom number defined better than the poissonian limit.

The experimental sequence used to characterize the noise properties of the imaging method is identical to that shown Fig. 8(a), except that in the fast imaging sequence we take only two images, each of duration τ . The atom number may be determined from a single imaging pulse by combining Eqs. (5) and (7). At the end of the i th imaging pulse, the atom number is given by

$$N_i = \frac{A}{\beta} \left[\frac{1 - e^{-\beta F_{\text{int}}/F_1}}{1 - e^{-A\tau}} \right], \quad (8)$$

and at the beginning of the pulse by

$$N_i^0 = \frac{A}{\beta} \left[\frac{e^{\beta F_{\text{int}}/F_1} - 1}{e^{A\tau} - 1} \right]. \quad (9)$$

The data set for this section comprises 100 experimental runs for each value of τ , with the exposure time sampled between

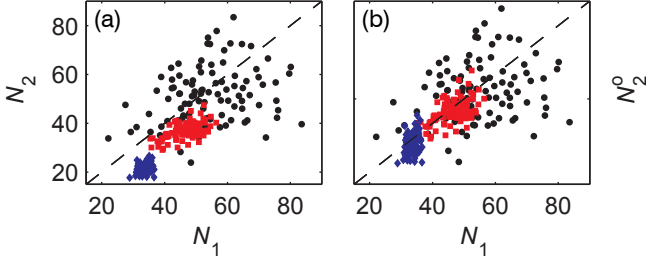


FIG. 9. (Color online) (a) Measured atom number at the end of pulse 1 and 2 for three imaging pulse durations: $\tau = 0.1$ ms (black circles), $\tau = 1$ ms (red squares), $\tau = 3$ ms (blue diamonds). The dashed line shows $N_2 = N_1$. (b) Same as (a), but we compare the atom number at the end of the first pulse N_1 and the number at the beginning of the second pulse N_2^0 inferred from the second pulse.

0.1 and 3 ms. The value of β was determined using the method of the previous section (see Fig. 8(b) and associated text), where the integrated fluorescence for each setting of τ was found by averaging the signal over the 100 experimental runs; the obtained value was $\beta = 4.94 \text{ s}^{-1}$. The initial atom number for the data set was gaussian distributed with mean value 62.5 and a standard deviation of 8.5 due to fluctuations in the loading process; this was obtained from averaging N_1^0 obtained from Eq. (9) over the data set.

The noise properties of the measured atom number changes as a function of the exposure time. Figure 9(a) shows the measured atom number N_2 v N_1 for three values of the pulse duration. For the shortest pulse duration, the signal shows a large degree of scatter; in this regime, the shot noise of the detected light is the dominant noise source. For longer pulse durations, the scatter decreases markedly but the mean atom loss during the second imaging pulse causes the data to deviate from the line $N_2 = N_1$. Figure 9(b) shows N_2^0 v N_1 . Given that N_1 and N_2^0 are measurements of the same atom number, the data lies on the line $N_2 = N_1$. However, the inferred atom number at the start of the second pulse shows a larger scatter than N_1 . To understand this behaviour, we model the noise in the measured atom number arising from the shot noise in the detected light and the loss of atoms during the imaging process.

The light shot noise contribution to the atom number variance may be found through standard error propagation. In particular, the variance in the atom number at the end of an imaging pulse due to light shot noise is given by $\sigma_{N_i}^2 = (dN_i/dF_{\text{int}})^2 \sigma_{F_{\text{int}}}^2 + (dN_i/dF_1)^2 \sigma_{F_1}^2$, assuming negligible uncertainty in the values of β and γ . A comparison of the two remaining terms in the error propagation formula shows that the term proportional to $\sigma_{F_1}^2$ is also negligible. Thus, $(dN_i/dF_{\text{int}})^2 \sigma_{F_{\text{int}}}^2$ gives the variance of the atom number arising from the light shot noise in pulse i . In principle, $\sigma_{F_{\text{int}}}^2 = g^2 \eta N_{\text{ph}} = g F_{\text{int}}$ (see discussion of the camera in Sec. II). However, due to the spatial variation in the photon scattering rate for an atom moving in the microtrap and imaging light, and the excess noise induced by the EMCCD camera, $\sigma_{F_{\text{int}}}^2 = \alpha F_{\text{int}}$, where $\alpha \approx 110$ and is determined from the histogram of ADU counts for a single atom exposed to the same imaging conditions. Despite the light shielding

of the apparatus, the background signal is also finite so that it makes a contribution σ_0^2 to the variance of the integrated signal: $\sigma_{F_{\text{int}}}^2 = \alpha F_{\text{int}} + \sigma_0^2$, where both terms depend on the exposure time.

To model atom loss during the imaging pulses, we perform a Monte-Carlo simulation based on the master equation of Eq. (3). The atom number distribution at the end of the first imaging pulse is obtained by solving Eq. (3) using the initial conditions obtained from the experiment. At time τ , the atom number is sampled and rounded to the nearest integer to give N_1 ; this atom number is then used as the initial condition for the atom number distribution's evolution during the second imaging pulse. The resulting probability distribution is sampled to obtain N_2 . This procedure is repeated 1000 times for each value of τ , from which we calculate the two-sample variance due to atom loss, σ_{Loss}^2 . To evaluate the noise properties of the method when comparing N_1 and N_2^0 , the sampled value of N_2 is inserted into Eq. (5) and rearranged to yield N_2^0 , whereupon we evaluate the two-sample variance $\frac{1}{2} \text{var}(N_2^0 - N_1)$.

Figure 10(a) shows the two-sample variance as a function of exposure time for N_1 and N_2 . Also shown is the two-sample variance predicted by the noise model $\sigma^2 = \sigma_{N_1}^2 + \sigma_{N_2}^2 + \sigma_{\text{Loss}}^2$. As in Fig. 9(a), the scatter of the experimental points initially decreases with the exposure time and reaches its minimum at $\tau \approx 0.4$ ms. The noise model shows that the noise contributions from the light and the atom loss are approximately equal at this point. For larger τ , the atom loss becomes the dominant noise source and the two-sample variance increases. In a small interval of τ values around 0.4 ms, the two-sample variance in detected atom number lies below the level of poissonian fluctuations. For exposure times longer than 3 ms, the two-sample variance again decreases due to two effects arising from the evolution of the atom number distribution: The first stems from the decreased loss rate at late times, meaning that the relative difference in mean atom number $\bar{N}_2 - \bar{N}_1$ is smaller than for low τ (see Fig. 7(a)); the second arises from the reduced variance in N_1 and N_2 at late times due to light-assisted collisions (see Figs. 7(b) and (c)).

The two-sample variance associated with N_1 and N_2^0 is shown in Fig. 10(b). The variance predicted by the noise model is given by $\sigma^2 = \sigma_{N_1}^2 + \sigma_{N_2^0}^2 + \sigma_{\text{Loss}}^2$. In the absence of the atom number variance associated with mean atom loss, the light shot noise is the dominant noise source until $\tau \approx 1$ ms, and remains finite at higher τ , consistent with Fig. 9(b) where it is apparent that the operation of Eq. (9) to obtain N_2^0 leads to increased variance. Nonetheless, for all exposure times above $\tau = 0.1$ ms, the imaging technique leads to a two-sample variance well-below the level of poissonian fluctuations. Indeed, for $0.75 \leq \tau \leq 3$ ms, the two-sample variance lies a factor of three to four below the poissonian limit, which is remarkable given the very high density of the atomic sample.

In calculating the two-sample variance for N_1 and N_2^0 , the use of process 1 in the noise model yields a significantly lower value of noise than the case of process 2, whereas for N_1 and N_2 , the two loss processes give rise to approximately the same noise level. This arises from the fact that the two-sample vari-

VI. CONCLUSION AND OUTLOOK

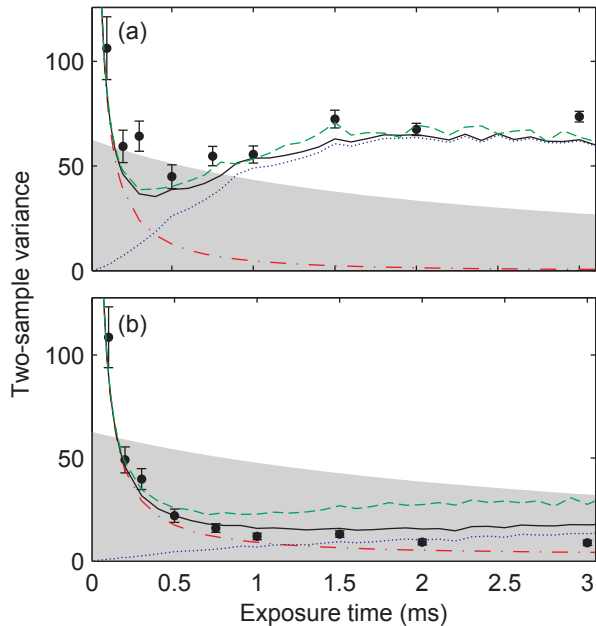


FIG. 10. (Color online) (a) Two-sample variance of N_1 and N_2 as a function of exposure time. (Black circles) Experimental data, error bars show 2σ statistical error, (red dash-dot line) calculated light noise $\sigma_{N_1}^2 + \sigma_{N_2}^2$, (blue dotted line) calculated noise arising from atom loss σ_{Loss}^2 based on Eq. (3) using process 1, (black solid line) calculated total noise $\sigma^2 = \sigma_{N_1}^2 + \sigma_{N_2}^2 + \sigma_{\text{Loss}}^2$ using process 1, (green dashed line) calculated total noise model using process 2. The shaded region indicates the interval where the atom number variance lies below the level of poissonian fluctuations. (b) Same as (a), but for N_1 and N_2^0 .

ance for N_1 and N_2 is dominated by the mean atom loss, so that the contribution from the widths of the atom number distributions is small. In contrast, by comparing N_1 and N_2^0 we remove the contribution of mean atom loss to the two-sample variance, whereby the choice of loss mechanism becomes the determining factor. As shown in Fig. 7, process 2 leads to a broader number distribution than process 1. Thus, process 2 leads to a larger uncertainty in atom number N_2 , which is amplified by the inversion of Eq. (9) to obtain N_2^0 .

The experimental data in Fig. 10(b) is better matched by the noise model assuming process 1, implying that this process is the dominant loss mechanism. As noted above, however, an experiment with just two atoms showed that process 1 and 2 occur with approximately equal probability. A partial explanation for this discrepancy could lie in the heating of the sample due to the high rate of inelastic collisions when probing many atoms in a dense sample: In [44] we found that an increase in sample temperature led to a higher probability for process 1 in inelastic collisions that release an energy less than the trap depth. Finally, at large exposure times, the experimental two-sample variance lies slightly below that predicted by process 1, indicating that there may be effects that are not captured by the noise model.

We have demonstrated a method of in-trap fluorescence imaging based on a standing wave of light that is blue-detuned from atomic resonance. In general, imaging in red-detuned dipole traps is complicated by the multitude of atomic energy levels and their different light shifts induced by the dipole trap beam(s). Here, given the use of probe light tuned to the blue of the uppermost hyperfine level, $F' = 3$ on the D1 line of ^{85}Rb , the probe has the greatest effect at the center of the trap, meaning that a two-level atom picture is sufficient. By combining the standing wave probe beam with a standard set of MOT cooling beams, we achieve a single atom detection probability of approximately 99% for a wide range of experimental parameters.

We have explored several features of single-atom detection using this method including the role of detuning for the probe and MOT cooling beams, and the intensity dependence of the Sisyphus cooling mechanism. The use of single atoms to characterize the method was important to avoid spurious results arising from the single-atom loss caused by the detection process.

The method was extended to the detection of up to ~ 100 atoms held in the microtrap, at densities exceeding 10^{13} cm^{-3} . When imaging such high-density samples in a trap of finite depth, inelastic two-body light-assisted collisions comprise the dominant loss mechanism. We mitigated this loss by using a blue-detuned probe beam. The effect of the small blue detuning is two-fold: It reduces the rate of inelastic light-assisted collisions via optical shielding, and, when an inelastic collision occurs, it limits the energy gained by the colliding atom pair to the detuning of the imaging light. By choosing the trap depth to be much larger than the energy gained in an inelastic collision, we achieved very small two-body loss rates β for such a dense sample. Indeed, the obtained values of the two-body loss rate, normalized to take account of the microscopic volume of the atomic sample, were two orders of magnitude smaller than those obtained using the standard approach of fluorescence detection based on red-detuned molasses light.

We modelled the effects of one- and two-body loss on the sample using a master equation to determine the atom number as a function of imaging time. For two-body loss, we considered two loss ‘‘channels’’: Process 1, where one atom is lost from the trap due to a binary light-assisted collision, and process 2, where both atoms are lost. These two processes lead to different atom number distributions in the trap, the signature of which was evident in the noise analysis of the imaging method. The method leads to the preparation and determination of the atom number up to a factor of four below the poissonian limit. When combined with internal state preparation, this method can be used to generate mesoscopic atomic samples useful for quantum information processing.

ACKNOWLEDGMENTS

This work is supported by the Marsden Fund and UORG. The authors thank T. Grünzweig and M. McGovern for their

important contributions at an early stage of the experiment and for comments on the manuscript.

-
- [1] R. Bourgain, J. Pellegrino, A. Fuhrmanek, Y. R. P. Sortais, and A. Browaeys, *Phys. Rev. A* **88**, 023428 (2013).
- [2] M. Saffman, T. G. Walker, and K. Mølmer, *Rev. Mod. Phys.* **82**, 2313 (2010).
- [3] J. D. Pritchard, D. Maxwell, A. Gauguier, K. J. Weatherill, M. P. A. Jones, and C. S. Adams, *Phys. Rev. Lett.* **105**, 193603 (2010).
- [4] V. Parigi, E. Bimbard, J. Stanojevic, A. J. Hilliard, F. Nogrette, R. Tualle-Brouri, A. Ourjoumtef, and P. Grangier, *Phys. Rev. Lett.* **109**, 233602 (2012).
- [5] M. Ebert, A. Gill, M. Gibbons, X. Zhang, M. Saffman, and T. G. Walker, *Phys. Rev. Lett.* **112**, 043602 (2014).
- [6] N. Schlosser, G. Reymond, I. Protchenko, and P. Grangier, *Nature* **411**, 1024 (2001).
- [7] J. F. Sherson, C. Weitenberg, M. Endres, M. Cheneau, I. Bloch, and S. Kuhr, *Nature* **467**, 68 (2010).
- [8] J. Weiner, *Cold and ultracold collisions in quantum microscopic and mesoscopic systems* (Cambridge University Press, 2003).
- [9] S. A. Aljunid, M. K. Tey, B. Chng, T. Liew, G. Maslennikov, V. Scarani, and C. Kurtsiefer, *Phys. Rev. Lett.* **103**, 153601 (2009).
- [10] A. Fuhrmanek, Y. R. P. Sortais, P. Grangier, and A. Browaeys, *Phys. Rev. A* **82**, 023623 (2010).
- [11] Z. Hu and H. J. Kimble, *Optics Letters* **19**, 1888 (1994).
- [12] S. Kuhr, W. Alt, D. Schrader, M. Müller, V. Gomer, and D. Meschede, *Science* **293**, 278 (2001).
- [13] C.-S. Chuu, F. Schreck, T. P. Meyrath, J. L. Hanssen, G. N. Price, and M. G. Raizen, *Phys. Rev. Lett.* **95**, 260403 (2005).
- [14] F. Serwane, G. Zürn, T. Lompe, T. B. Ottenstein, A. N. Wenz, and S. Jochim, *Science* **332**, 336 (2011).
- [15] D. B. Hume, I. Stroescu, M. Joos, W. Muessel, H. Strobel, and M. K. Oberthaler, *Phys. Rev. Lett.* **111**, 253001 (2013).
- [16] M. McGovern, A. J. Hilliard, T. Grünzweig, and M. F. Andersen, *Opt. Lett.* **36**, 1041 (2011).
- [17] J. Dalibard and C. Cohen-Tannoudji, *J. Opt. Soc. Am. B* **2**, 1707 (1985).
- [18] A. Aspect, J. Dalibard, A. Heidmann, C. Salomon, and C. Cohen-Tannoudji, *Phys. Rev. Lett.* **57**, 1688 (1986).
- [19] S. Bali, D. Hoffmann, and T. Walker, *EPL (Europhysics Letters)* **27**, 273 (1994).
- [20] J. Weiner, V. S. Bagnato, S. Zilio, and P. S. Julienne, *Rev. Mod. Phys.* **71**, 1 (1999).
- [21] J. Hynczek and T. Nishiwaki, *Electron Devices, IEEE Transactions on*, *Electron Devices*, *IEEE Transactions* **50**, 239 (2003).
- [22] M. S. Robbins and B. J. Hadwen, *IEEE Transactions on Electron Devices* **50**, 1227 (2003).
- [23] The stochastic gain of the EMCCD leads to the fact that these ‘dark’ regions, rather than showing a symmetric histogram of counts centered around a mean background level, instead have an asymmetric histogram characteristic of an extreme value distribution, where the tail of the distribution is longer towards higher counts. We take the peak value of this histogram, i.e., the mode of the distribution, as the background level we subtract from the atomic signal. This leads to a small, positive bias on our images.
- [24] T. Grünzweig, A. Hilliard, M. McGovern, and M. F. Andersen, *Nat Phys* **6**, 951 (2010).
- [25] A. V. Carpentier, Y. H. Fung, P. Sompet, A. J. Hilliard, T. G. Walker, and M. F. Andersen, *Laser Physics Letters* **10**, 125501 (2013).
- [26] C.-Y. Shih and M. S. Chapman, *Phys. Rev. A* **87**, 063408 (2013).
- [27] R. Grimm, M. Weidemüller, and Y. B. Ovchinnikov, *Advances In Atomic, Molecular, and Optical Physics* **42**, 95 (2000).
- [28] B. W. Shore, *The Theory of Coherent Atomic Excitation*, Vol. 1 (John Wiley & Sons, Inc., 1990).
- [29] D. A. Steck, “Rubidium 85 D Line Data,” <http://steck.us/alkalidata>.
- [30] We neglect the contributions from other spectral lines in ^{85}Rb , of which the strongest are the $5^2\text{S}_{1/2}$ to $6^2\text{P}_{1/2}$ and $6^2\text{P}_{3/2}$ lines at ~ 420 nm, and the $5^2\text{P}_{1/2}$ and $5^2\text{P}_{3/2}$ to $4^2\text{D}_{3/2}$ lines at 1475 nm and 1529 nm respectively. This is a very good approximation given how close the wavelength of the dipole trap is to those of the $5^2\text{S}_{1/2}$ to $5^2\text{P}_{1/2}$ and $5^2\text{P}_{3/2}$ lines, and the fact that these transitions are at minimum a factor of 45 stronger than the next most intense. See J. E. Sansonetti, *J. Phys. Chem. Ref. Data*. **35**, 301 (2006).
- [31] M. O. Scully and M. S. Zubairy, *Quantum Optics* (Cambridge University Press, 1997).
- [32] A. L. Stancik and E. B. Brauns, *Vibrational Spectroscopy* **47**, 66 (2008).
- [33] H. J. Metcalf and P. van der Straten, *Laser Cooling and Trapping*, 1st ed. (Springer, 1999).
- [34] D. J. Wineland, J. Dalibard, and C. Cohen-Tannoudji, *J. Opt. Soc. Am. B* **9**, 32 (1992).
- [35] Y. R. P. Sortais, A. Fuhrmanek, R. Bourgain, and A. Browaeys, *Phys. Rev. A* **85**, 035403 (2012).
- [36] N. G. van Kampen, *Stochastic Processes in Physics and Chemistry*, 3rd ed. (Elsevier, Amsterdam), 2007).
- [37] S. Whitlock, C. F. Ockeloen, and R. J. C. Spreeuw, *Phys. Rev. Lett.* **104**, 120402 (2010).
- [38] For instance, to load a small number of atoms into the micro-trap, we shorten the MOT loading time to ~ 500 ms, and reduce the magnetic field gradient and the duration of the CMOT phase. This procedure leads to a shot-to-shot variation of about 10% in the loaded atom number once the experiment is thermally stable. Alternatively, one can leave the experimental parameters for loading constant and then drive inelastic light-assisted collisions to reduce the atom number. However, by this method, the temperature of the atomic sample is increased.
- [39] Note that by working with the cumulative signal, the method is also applicable using a camera operated in a standard mode, i.e., a camera without the ability to take several images in quick succession.
- [40] A. Fuhrmanek, R. Bourgain, Y. R. P. Sortais, and A. Browaeys, *Phys. Rev. A* **85**, 062708 (2012).
- [41] See Ref. [40] for a brief survey of measured values of β found in the literature.
- [42] J. Pellegrino, R. Bourgain, S. Jennewein, Y. R. P. Sortais,

- A. Browaeys, S. D. Jenkins, and J. Ruostekoski, Phys. Rev. Lett. **113**, 133602 (2014).
- [43] H. Zhang, R. McConnell, S. Čuk, Q. Lin, M. H. Schleier-Smith, I. D. Leroux, and V. Vuletić, Phys. Rev. Lett. **109**, 133603 (2012).
- [44] P. Sompet, A. V. Carpentier, Y. H. Fung, M. McGovern, and M. F. Andersen, Phys. Rev. A **88**, 051401 (2013).